

Ionizing feedback from massive stars in massive clusters – II. Disruption of bound clusters by photoionization

J. E. Dale,^{1*} B. Ercolano¹ and I. A. Bonnell²

¹*Excellence Cluster ‘Universe’, Boltzmannstr. 2, 85748 Garching, Germany*

²*Department of Physics and Astronomy, University of St Andrews, North Haugh, St Andrews, Fife KY16 9SS*

Accepted 2012 April 27. Received 2012 April 27; in original form 2011 October 16

ABSTRACT

We present a smoothed particle hydrodynamics parameter study of the dynamical effect of photoionization from O-type stars on star-forming clouds of a range of masses and sizes during the time window before supernovae explode. Our model clouds all have the same degree of turbulent support initially, the ratio of turbulent kinetic energy to gravitational potential energy being set to $E_{\text{kin}}/|E_{\text{pot}}| = 0.7$. We allow the clouds to form stars and study the dynamical effects of the ionizing radiation from the massive stars or clusters born within them. We find that dense filamentary structures and accretion flows limit the quantities of gas that can be ionized, particularly in the higher density clusters. More importantly, the higher escape velocities in our more massive ($10^6 M_{\odot}$) clouds prevent the H II regions from sweeping up and expelling significant quantities of gas, so that the most massive clouds are largely dynamically unaffected by ionizing feedback. However, feedback has a profound effect on the lower density 10^4 and $10^5 M_{\odot}$ clouds in our study, creating vast evacuated bubbles and expelling tens of per cent of the neutral gas in the 3-Myr time-scale before the first supernovae are expected to detonate, resulting in clouds highly porous to both photons and supernova ejecta.

Key words: stars: formation – H II regions.

1 INTRODUCTION

The vast majority of stars form in giant molecular clouds (GMCs) as members of embedded clusters (Lada & Lada 2003). By comparing birth rates of embedded clusters to the number of surviving open clusters, Lada & Lada (2003) concluded that up to 90 per cent of clusters are disrupted during their embedded phase. It has long been thought that GMCs and embedded clusters are initially gravitationally bound (e.g. Solomon, Sanders & Scoville 1979). These two observations can be reconciled if gas ejection by stellar feedback while the gas:stars mass ratio is large unbinds clouds and clusters by decreasing the gravitational potential too quickly for the clusters to adjust. Hills (1980) and later Goodwin (1997), Boily & Kroupa (2003a,b) and Goodwin & Bastian (2006) studied the effects of removing residual gas from embedded clusters at various rates. They showed that lower star formation efficiencies and shorter gas removal time-scales result in the unbinding of larger fractions of stars, up to the total disruption of clusters – a process often referred to as ‘infant mortality’. However, none of these authors modelled the gas removal process itself.

There are several feedback mechanisms which are thought to be able to influence the dynamics of whole molecular clouds such

as H II regions, winds, jets and supernovae. By considering the momentum injected by these various mechanisms, Matzner (2002) concluded that H II region expansion was the most important for clouds with masses $\gtrsim 10^5 M_{\odot}$. Analytical and numerical models of ionization-driven champagne flows (Bodenheimer, Tenorio-Tagle & Yorke 1979; Tenorio-Tagle 1979; Whitworth 1979; Williams & McKee 1997) have shown that they could be an efficient dispersal mechanism of uniform clouds if the massive stars were located near the peripheries of the clouds. In contrast, work by Mazurek (1980) and Yorke et al. (1989) showed that the dispersal efficiency was strongly reduced by the action of gravity or by placing the stars deep inside the clouds. GMCs have very complex density structures and turbulent velocity fields and clusters are usually found deeply embedded inside them. The massive stars in turn are usually to be found near cluster centres, either because they formed there through competitive accretion (e.g. Bonnell, Vine & Bate 2004) or migrated there through rapid mass segregation (e.g. McMillan, Vesperini & Portegies Zwart 2007; Allison et al. 2009; Moeckel & Bonnell 2009).

Several authors have modelled ionizing feedback from embedded massive stars on their parent molecular clouds. One-dimensional models of the evolution of 2×10^5 – $5 \times 10^6 M_{\odot}$ GMCs by Krumholz, Matzner & McKee (2006) concluded that H II regions would destroy clouds $\gtrsim 10^6 M_{\odot}$ on time-scales of ~ 30 Myr, corresponding to a few freefall times, whilst the lower mass clouds

*E-mail: dale@usm.lmu.de

would survive only ~ 10 Myr. Goldbaum et al. (2011) constructed semi-analytic models in which they examined the energy input in a GMC from both internal sources (H_{II} regions) and external sources (accretion of additional mass) and found that these two sources were of roughly equal importance in driving turbulence within the clouds. Dale et al. (2005) and Dale & Bonnell (2011) found that accretion flows on to the O-stars strongly limit the effect of radiation by only allowing it to escape into a small fraction of the sky as seen from each source. Peters et al. (2010) also found that the expansion of H_{II} regions could be limited by hydrodynamic flows. Walch et al. (2011) investigated the evolution of fractal molecular clouds with central ionizing sources. They show that the gas distribution prior to the ignition of the ionizing sources is of crucial importance in determining the outcome of the simulations, and that the principle effect of ionization is to enhance density contrasts that were already present. Vázquez-Semadeni et al. (2010) examine the effect of ionizing feedback on both accretion of material on to GMCs themselves, and on the star formation rates within. They find that feedback generally reduces the star formation efficiency, but that the effect is smaller for more massive and denser clouds.

The works cited above have only examined a limited portion of the parameter space of possible GMCs. In this paper, we begin a parameter study where we construct undriven turbulent molecular clouds with a variety of masses and radii, allow them to form stars, and model the effects of the photoionizing feedback from their stellar populations. Heyer et al. (2009) have re-examined the data from Solomon et al. (1987) and produced a catalogue of masses, radii and velocity dispersions for 158 clouds which we use to define the mass–radius parameter space for this study. As pointed out by Dobbs, Burkert & Pringle (2011), most of the clouds in Heyer et al. (2009)’s catalogue are in fact not gravitationally bound, in contradiction to the common assumption about star-forming GMCs. However, the virial ratio of the clouds in the Heyer et al. (2009) sample is not independent of cloud mass, but instead declines with increasing mass, so that more massive clouds are more likely to be bound, and in fact very few clouds with masses in excess of $10^4 M_{\odot}$ were found to be unbound by Dobbs et al. (2011). Since the cloud mass function is rather shallow, with a power-law slope of ~ -1.6 to -1.8 , the massive objects, although less numerous, contain most of the total mass. Unbound clouds may be common by number, but most mass resides in clouds that are bound. Therefore, in this study we restrict ourselves to studying clouds where the ratio of turbulent kinetic to potential energy is less than unity. To begin with, we reduce the size of the parameter space by insisting that all clouds have the same degree of initial turbulent support with the ratio $E_{\text{kin}}/|E_{\text{pot}}|$ set to 0.7, chosen so that each cloud would be roughly midway between virial equilibrium and marginal boundedness if the turbulent kinetic energy were the only means of support. Our aim in this is to answer the question of whether ionizing feedback can in principle disrupt bound molecular clouds and terminate star formation inside them. We will extend the parameter space to include clouds in which the turbulent kinetic energy exceeds the potential energy in later work.

We describe our numerical techniques in Section 2, present our results in Section 3 and our discussion and conclusions follow in Sections 4 and 5, respectively.

2 NUMERICAL METHODS

We use a well-known variant of the Benz (Benz 1990) smoothed particle hydrodynamics (SPH; Monaghan 1992) code, which is ideal for studying the evolution of molecular clouds and embedded clus-

ters. In all our simulations, we begin with 10^6 gas particles. We use the standard artificial viscosity prescription, with $\alpha = 1$, $\beta = 2$. Particles are evolved on individual time-steps. The code is a hybrid N -body SPH code in which stars are represented by point-mass sink particles (Bate, Bonnell & Price 1995). Self-gravitational forces between gas particles are calculated using a binary tree, whereas gravitational forces involving sink particles are computed by direct summation. Sink particles are formed dynamically and may accrete gas particles and grow in mass. In our simulations of 10^5 and $10^6 M_{\odot}$ clouds, the sink particles represent stellar clusters, since the mass resolution is not sufficient to capture individual stars. The accretion radii of the clusters are chosen to be 0.25 pc in our Runs A, B, X and D and 0.1 pc in Runs E and F, so that the accretion radii of the sinks (our effective cluster radii) are always $\lesssim 1$ per cent of the radius of the simulated clouds. Clusters approaching each other to within their accretion radii are merged if they are mutually gravitationally bound. In our $10^4 M_{\odot}$ simulations, sink particles represent individual stars. Their accretion radii are set to 0.005 pc ($\sim 10^3$ au) and mergers are not permitted. In all simulations gravitational interactions of sink particles with other sink particles are smoothed within their accretion radii.

We treat the thermodynamics of the neutral gas using a piecewise barotropic equation of state (EOS) from Larson (2005). The use of a EOS is of course an approximation in lieu of either using prescribed heating and cooling functions or attempting extremely expensive full radiative transfer calculations, but the one we employ here broadly reproduces the findings of more sophisticated treatments of interstellar medium (ISM) thermodynamics. The EOS we have chosen was originally conceived by Larson (1985) based on observations of cloud temperatures and densities collected by Myers (1978) and was intended in particular to capture the increase in the gas cooling rate with increasing density at low densities, so that $T \sim \rho^{-0.3}$, until the gas becomes thermally coupled to the dust at a density of $\sim 10^{-19} \text{ g cm}^{-3}$. This EOS has proved to be a robust approximation in both atomic and molecular gas and has been recovered by several authors using either cooling and heating functions or performing radiative transfer calculations. Koyama & Inutsuka (2000) obtained a very similar temperature–density relation at densities below $\sim 2 \times 10^{-20} \text{ g cm}^{-3}$ based on thermal equilibrium calculations from Wolfire et al. (1995). Glover & Mac Low (2007), Glover et al. (2010) and Glover & Clark (2012) all recovered very similar temperature–density relations in studies of molecular cloud and star formation.

Our EOS is defined so that $P = k\rho^{\gamma}$, where

$$\begin{aligned} \gamma &= 0.75, & \rho &\leq \rho_1, \\ \gamma &= 1.0, & \rho_1 &\leq \rho \leq \rho_2, \\ \gamma &= 1.4, & \rho_2 &\leq \rho \leq \rho_3, \\ \gamma &= 1.0, & \rho &\geq \rho_3, \end{aligned} \tag{1}$$

and $\rho_1 = 5.5 \times 10^{-19} \text{ g cm}^{-3}$, $\rho_2 = 5.5 \times 10^{-15} \text{ g cm}^{-3}$ and $\rho_3 = 2 \times 10^{-13} \text{ g cm}^{-3}$. At low densities, γ is less than unity, which mimics the effects of line cooling and implicitly heats very low density gas above the canonical molecular gas temperature of ~ 10 K. The isothermal $\gamma = 1.0$ segment at moderate densities approximates the effect of dust cooling and the $\gamma = 1.4$ segment represents the regime where dense collapsing cores become optically thick and behave adiabatically. The final isothermal phase of the EOS is simply in order to allow sink particle formation to occur. Once the minimum gas temperature, which we set to 7.5 K, is specified, the relation

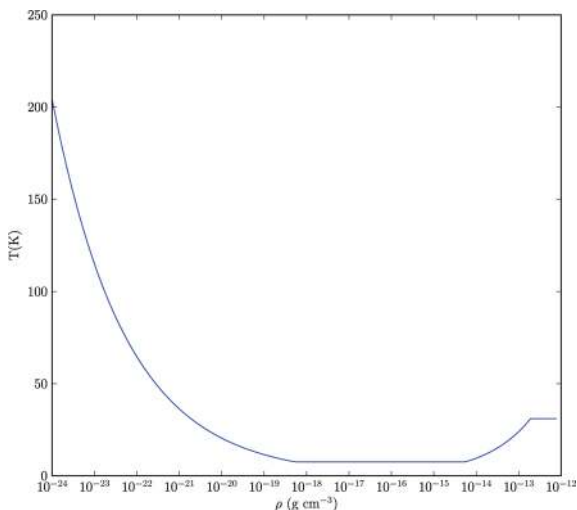


Figure 1. Relation between density and temperature used in our calculations.

between ρ and T , which we plot in Fig. 1, is fixed. All our simulated clouds have initial average densities $<\rho_1$, so that they lie initially in the line-cooling-dominated regime.

We use the photoionization code described in Dale, Ercolano & Clarke (2007) and Dale & Bonnell (2011). The code uses a simple ray-tracing algorithm and a Strömgren volume technique to compute the flux of ionizing photons arriving at a given SPH particle and update its ionization state accordingly. The on-the-spot approximation is used and the modified recombination coefficient α_B is taken to be $3.0 \times 10^{-13} \text{ cm}^3 \text{ s}^{-1}$. Fully ionized particles are given a temperature of 10^4 K , whereas partially ionized particles are given temperatures computed from multiplying their ionization fraction by 10^4 K . Ionized particles that are deprived of photons are allowed to recombine on their individual recombination time-scales. If their ionization fractions fall below 0.1, they are considered to be fully neutral once more and they are then allowed to descend the cooling curve from Schmutzler & Tscharnuter (1993).

The ionization algorithm was modified in a simple way in Dale & Bonnell (2011) to cope with the action of multiple ionizing sources with overlapping H II regions – we assumed in that work that if a given ionized particle of number density n was receiving photons from N sources, then the volume recombination rate as seen by each source was $\alpha_B n^2 N$. This approximation is rather crude and we have updated the algorithm to make it more physically realistic. In truth, the number of photons subtracted from the beams from each source passing through a multiply illuminated particle is proportional to the photon flux from each source as a fraction of the total flux passing through the particle. If an ionized particle is being illuminated by i sources and receives a photon flux F_i from each one, the volume recombination rate seen by each source is then $\alpha_B n^2 F_i / \sum F_i$. We have implemented this in a new version of our algorithm, which iterates, recomputing the individual and total fluxes received by all particles each time until the number of ionized particles converges to an accuracy of 0.1 per cent. We will describe this technique in detail in Dale & Ercolano (in preparation) and validate it by comparison with the Monte Carlo radiative transfer code MOCASSIN (Ercolano et al. 2003, 2008; Ercolano, Barlow & Storey 2005). As described below, we repeat the simulation from Dale & Bonnell (2011) using the new algorithm and compare the results, finding only minor differences in the dynamical influence of ionization.

In some of our clouds, our mass resolution is sufficient to regard sink particles as individual stars. We assign each star an ionizing photon flux dependent on its mass M_* . To reduce the number of low-mass, low-flux ionizing sources which are likely to slow down simulations but contribute few photons, we neglect ionizing sources with masses less than $20 M_\odot$. There is a knee in the relation between mass and ionizing luminosity at this mass, so that the total photon budget of a given stellar system will be dominated by stars whose masses exceed $20 M_\odot$. We assign photon fluxes according to the formula

$$\log(Q_{\text{H}}) = 48.1 + 0.02(M_* - 20 M_\odot), \quad (2)$$

an approximate fit to the ionizing photon fluxes of solar-metallicity stars tabulated in Diaz-Miller, Franco & Shore (1998).

In our simulations of higher mass clouds, our mass resolution is insufficient to follow the formation of individual stars and we instead treat the sink particles as small clusters. We use the criterion from Dale & Bonnell (2011) to determine their photon fluxes as follows. We compute, assuming a Salpeter mass function between 0.1 and $100 M_\odot$, the mass in stars of more than $30 M_\odot$ and divide this quantity by $30 M_\odot$ (assuming that such a star is a typical O-star). We then multiply this by the photon flux appropriate for this mass from the above formula, $\sim 2 \times 10^{48} \text{ s}^{-1}$ (not 10^{49} s^{-1} as incorrectly given in Dale & Bonnell 2011). This is evidently a very crude means of estimating the subclusters’ luminosities but any such estimate will be crude, since the form and limits of the mass function must be assumed. In addition, except for rather massive clusters, the high-mass end of the stellar mass function will be poorly sampled and the actual numbers and masses of O-stars are therefore very uncertain. We subsequently find, as shown in Appendix A, that uncertainties of a factor a few in the ionizing luminosities of our sources have very little influence on our results.

Our model clouds initially have a Gaussian three-dimensional density profile. We seed the gas with a Kolmogorov turbulent velocity field whose total kinetic energy is equal in magnitude to $7/10$ the cloud’s initial gravitational binding energy, so that the clouds would be bound if the thermal energy does not contribute significantly to the virial balance, and are therefore expected to form stars efficiently on their freefall time-scale in the absence of feedback.

3 EMBEDDED CLUSTER PARAMETER SPACE

Heyer et al. (2009) derived masses, radii and velocity dispersions for 158 molecular clouds ranging in radius from a few to $\sim 100 \text{ pc}$ and in mass from $\sim 10^3$ to $\sim 10^6 M_\odot$. We chose the sizes and masses of our clouds to cover the higher mass end of Heyer et al. (2009)’s data set, since GMC’s with masses of $10^3 M_\odot$ will not form many O-stars. We therefore study clouds in the mass range 10^4 – $10^6 M_\odot$, covering systems from approximately the size of Orion to 30 Doradus. We choose cloud radii in the range 5–a few $\times 10^2 \text{ pc}$, resulting in freefall times of between 0.8 and 20 Myr. We choose initial turbulent velocities to be in the range 1–10 km s^{-1} so that all of our clouds have the same ratio $E_{\text{kin}}/|E_{\text{pot}}|$ of 0.7. In Figs 2 and 3 mass–radius and mass–velocity dispersion plots with our simulated clusters overlaid on the data from Heyer et al. (2009), showing that our clouds overlap nicely the parameters of observed star-forming clouds. In Fig. 4, we plot the mass–radius parameter space with colours and black contour lines overlaid representing the velocity required to give each cluster our chosen initial virial ratio.

This picture is complicated somewhat by our EOS. If we were to make the simple canonical assumption that the gas in our clouds is purely isothermal with an average temperature of 10 K, the thermal

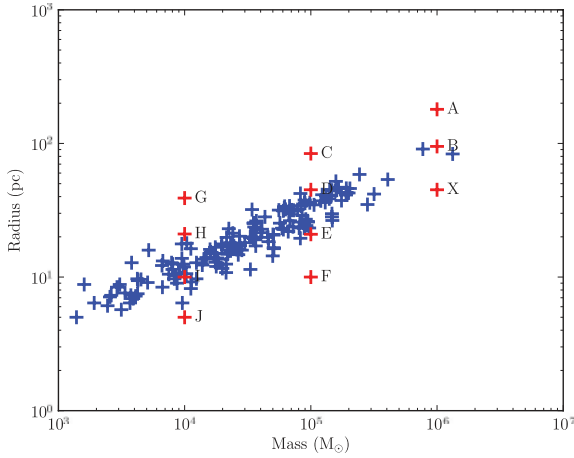


Figure 2. Cluster mass–radius parameter space with clouds from Heyer et al. (2009) plotted as blue crosses and our model clouds plotted as red crosses.

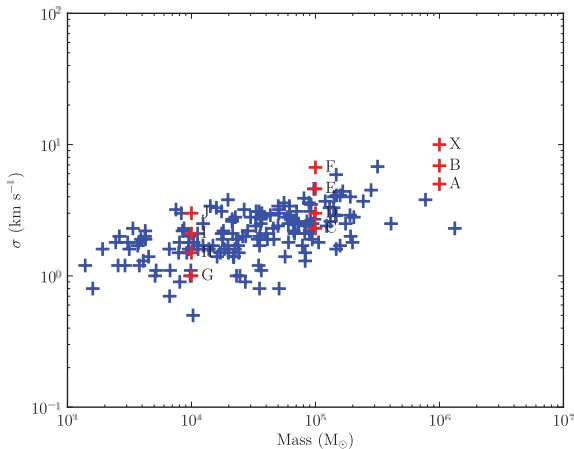


Figure 3. Cluster mass–velocity dispersion parameter space with clouds from Heyer et al. (2009) plotted as blue crosses and our model clouds plotted as red crosses.

energy would make a negligible contribution to the clouds’ energy balance in all cases. This is not necessarily true when we make use of the more realistic Larson EOS, since the gas densities are initially low enough that the gas is in the warm non-isothermal regime, so that the contribution of the thermal energy may become important.

In Table 1 we give the total mass, initial radius, initial rms turbulent velocity, initial mean number density (assumed to be molecular), freefall time, mean initial temperature and true virial ratio (including the thermal energy) of all of our clouds (mean quantities are mass-weighted). The initial mean temperatures of several of the clouds are very high and, in the case of Runs G and H, the initial thermal energy of the cloud is large enough that the clouds are not initially bound. In the cases of clouds A, C and G, the initial mean temperatures are sufficiently high that the clouds should more properly be regarded as atomic and not molecular. However, all these clouds are seeded with supersonic turbulent velocity fields which will shock the gas, locally increasing the density and decreasing the temperature. It is therefore not obvious simply from the contents of Table 1 that even the warmest clouds will not form at least some stars.

For those clouds that are able to form stars, we model the effect of ionization feedback. Photoionization and winds act for the whole

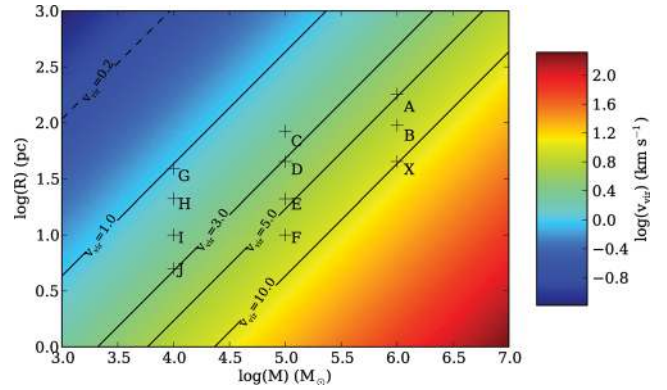


Figure 4. Cluster mass–radius parameter space studied in this work. Colours and black contour lines are velocities required to give uniform clusters of given mass and radius a ratio $E_{\text{kin}}/|E_{\text{pot}}|$ of 0.7.

duration of a massive star’s lifetime, whereas supernovae are isolated events occurring at the end of that lifetime. The influence of feedback is likely to be dominated by the most massive stars, which have main-sequence lifetimes of ~ 3 Myr. This sets the time-scale on which photoionization and winds can modify GMCs before the action of supernovae. In about half the clouds studied here – runs X, E, F, I and J – the cloud freefall time is less than or comparable to 3 Myr, which we will refer to in future as t_{SN} . If star formation is to go to completion and these clouds be disrupted in a few crossing times, most or all of the work must be done by photoionization and winds/jets (note that we defer the study of the effects of winds to a later paper).

4 REGULATION OF PHOTOIONIZING FEEDBACK

There are at first sight three issues which determine how strong the effects of ionizing feedback may be on a given cluster.

(i) *Number and luminosity of ionizing sources.* The number of ionizing sources present at a given time in a cluster’s evolution depends on the mass function and the total stellar mass. The dominant sources of ionizing feedback are the most massive stars or clusters and, since the stellar and cluster mass functions are steep power laws, their high-mass ends are likely to be poorly sampled and subject to stochastic effects whereby a small change in the initial conditions or input physics may result in the same quantity of mass being distributed amongst different numbers and (therefore masses) of individual objects. Since the ionizing luminosity of stars and clusters are rather strong functions of their masses, this may in principle lead to statistical uncertainties in the total ionizing flux and how the sources are distributed at a given time in a simulation. In an attempt to eliminate some of the stochasticity inherent in star formation we do not enable ionization by clusters in our 10^5 and $10^6 M_{\odot}$ calculations until, respectively, three and 10 clusters hosting at least one O-star have formed, and in the $10^4 M_{\odot}$ runs until three ionizing sources have formed. We subsequently find, as detailed in Appendix A, that allowing ionization to begin as soon as any ionizing sources have formed actually does not strongly affect the results. The reason for this is largely that variations of a factor of a few in the ionizing luminosity at any given time do not strongly affect the evolution of our clouds, as also shown explicitly in Appendix A.

(ii) *The ability of sources to ionize fresh gas.* The rate at which new material is ionized is expected to depend strongly on the

Table 1. Initial properties (mass, radius, turbulent velocity dispersion, mean initial molecular number density, freefall time, mean initial temperature and virial ratio) of all runs.

Run	Mass (M_{\odot})	Radius (pc)	v_{rms} (km s^{-1})	$\langle n(\text{H}_2) \rangle$ (cm^{-3})	t_{ff} (Myr)	$\langle T \rangle$ (K)	$(E_{\text{kin}} + E_{\text{therm}})/ E_{\text{pot}} $
A	10^6	180	5.0	2.9	19.6	143	0.72
B	10^6	95	6.9	16	7.50	91	0.70
X	10^6	45	9.6	149	2.44	52	0.69
C	10^5	84	2.3	2.6	19.7	145	0.90
D	10^5	45	3.0	15	7.70	92	0.78
E	10^5	21	4.6	147	2.46	52	0.71
F	10^5	10	6.7	1439	0.81	30	0.69
G	10^4	39	1.0	2.2	19.7	149	1.92
H	10^4	21	1.5	14	7.79	93	1.10
I	10^4	10	2.1	136	2.56	53	0.79
J	10^4	5	3.0	1135	0.90	32	0.72

ambient gas density and on the strength of accretion flows which may swamp ionizing sources with neutral material (e.g. Peters et al. 2010; Dale & Bonnell 2011). Walmsley (1995) gives a simple formula for a critical accretion rate \dot{M}_{crit} on to an ionizing source of mass M and ionizing luminosity Q_{H} (Lyman continuum photons per second) above which all the ionizing photons are absorbed by the accretion flow, so that the H II region cannot expand and may instead contract:

$$\dot{M} > \left(\frac{4\pi Q_{\text{H}} G M m_{\text{H}}^2}{\alpha_{\text{B}}} \right)^{1/2}. \quad (3)$$

The accretion rate on to a given source depends on the ambient gas density and may be roughly estimated from the Bondi accretion rate \dot{M}_{B} , given by

$$\dot{M}_{\text{B}} = \frac{4\pi G^2 M^2 \rho}{c_{\text{s}}^3}. \quad (4)$$

If we crudely set $\dot{M}_{\text{crit}} = \dot{M}_{\text{B}}$ and set $c_{\text{s}} = c_{\text{II}}$ (the speed of sound in ionized gas), we obtain the condition that, for an accretion flow to swamp an ionizing source

$$\frac{GM}{c_{\text{II}}^2} > \left(\frac{Q_{\text{H}}}{4\pi n^2 \alpha_{\text{B}}} \right)^{1/3}, \quad (5)$$

which is, to within a factor close to unity, the same as saying that the radius at which the escape velocity exceeds the sound speed in the ionized gas must exceed the Strömgen radius in order for the H II region to be trapped. (Note that we do not artificially shut off sources whose accretion rates exceed these critical values – all ionizing sources are left to contend with their accretion flows self-consistently.)

(iii) *The ability of ionized gas to expel neutral material.* Unless a cluster’s O-stars are able to ionize its entire reserve of neutral gas, the ability of the massive stars to disrupt the system will depend on how effectively the expanding H II regions can sweep up neutral material. This in turn depends largely on the escape velocity of the system as a whole (as opposed to the escape velocity of individual stars or subclusters, which governs how much gas is likely to be ionized) compared to the sound speed in ionized gas. In Fig. 5, we plot the variation in escape velocity across our parameter space, with a contour indicating c_{II} which we take to be 10 km s^{-1} . Evidently, some of the denser clusters in the parameter space have such high escape velocities that ionization will struggle to expel gas from them.

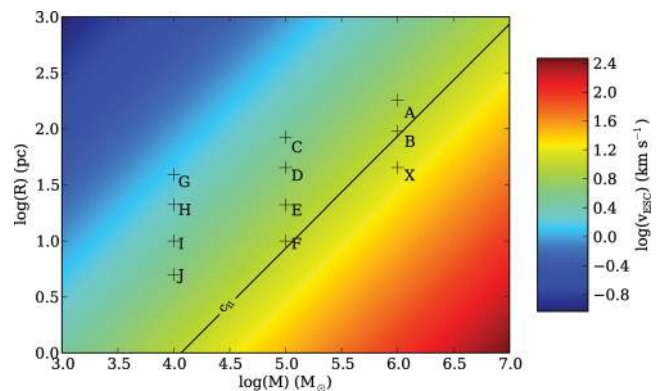


Figure 5. Escape velocities of clusters studied in this work.

5 EFFECTS OF PHOTOIONIZATION ON MODEL CLUSTERS

The effects of photoionization in the t_{SN} time window before the first supernovae are expected to detonate vary strongly across our parameter space. There is a general gradient pointing from the denser massive, high- v_{rms} clusters, to which it does little, towards the lower density low-mass, low- v_{rms} clusters, to which it is extremely disruptive. In Fig. 6, we show a gallery of the state of the clusters at the time when ionization is enabled. In Runs C, G and H, the implicit heating of the piecewise EOS and the low turbulent velocities combine to prevent star formation. The high mean gas temperatures raise the thermal energy of these clouds so that clouds G and H are unbound and cloud C is nearly so. Furthermore, the low turbulent velocity dispersions and high temperatures result in mean Mach numbers so low that the turbulence dissipates without producing any very strong enhancements in the clouds’ density fields. These clouds warm up and expand without forming any gravitationally unstable structures.

All the other clouds undergo star formation on time-scales comparable to their freefall times. The impact of feedback varies strongly across the parameter space and we find that it is the lower density star-forming clouds which are most strongly affected. Since these are also the warmer clouds, we repeated several simulations (Runs A, D, E and I) using an isothermal EOS with a uniform temperature of 10 K to evaluate the impact of the EOS on our results. We find that this change makes little difference to the outcome of the simulations.

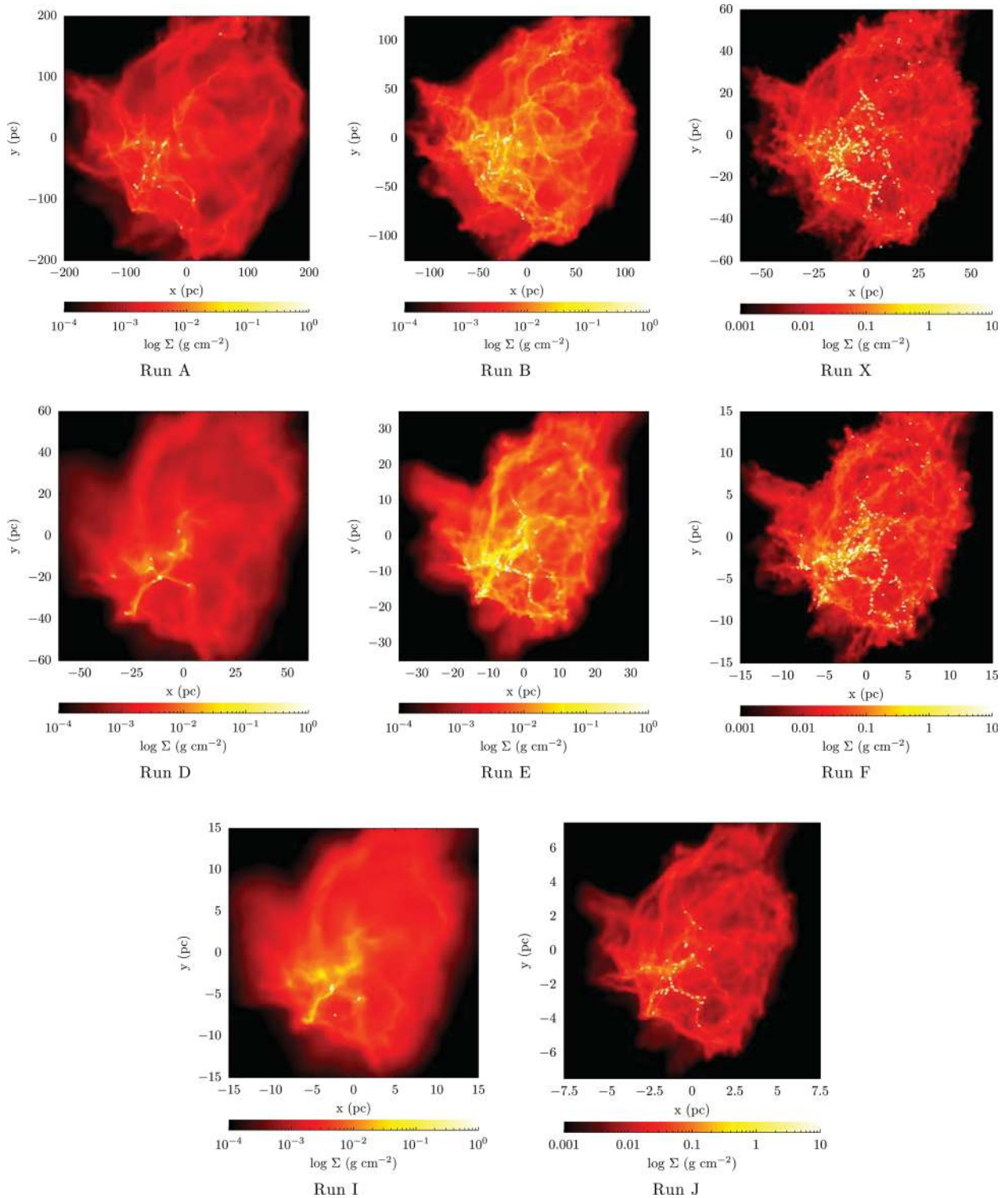


Figure 6. Gallery of initial conditions of clusters, as shown by column density maps observed down the z -axis. White dots represent sink particles (individual stars in Runs I and J, clusters otherwise) and are not to scale. Note the different physical sizes and the different column density scales.

All the systems have the same turbulent velocity field but different v_{rms} , so that many structures in the gas are visible in all simulations. All the systems exhibit a filamentary structure, with star formation being largely confined to the filaments and particularly to junctions connecting several filaments. This morphology is very similar to that

observed increasingly frequently in cold dust emission by Herschel (e.g. André et al. 2010; Men'shchikov et al. 2010; Hill et al. 2011). However, it is clear that the filamentary features in the gas are more sharply defined and complex in the systems with higher v_{rms} , higher mean densities and lower average temperatures (e.g. Runs B, X and

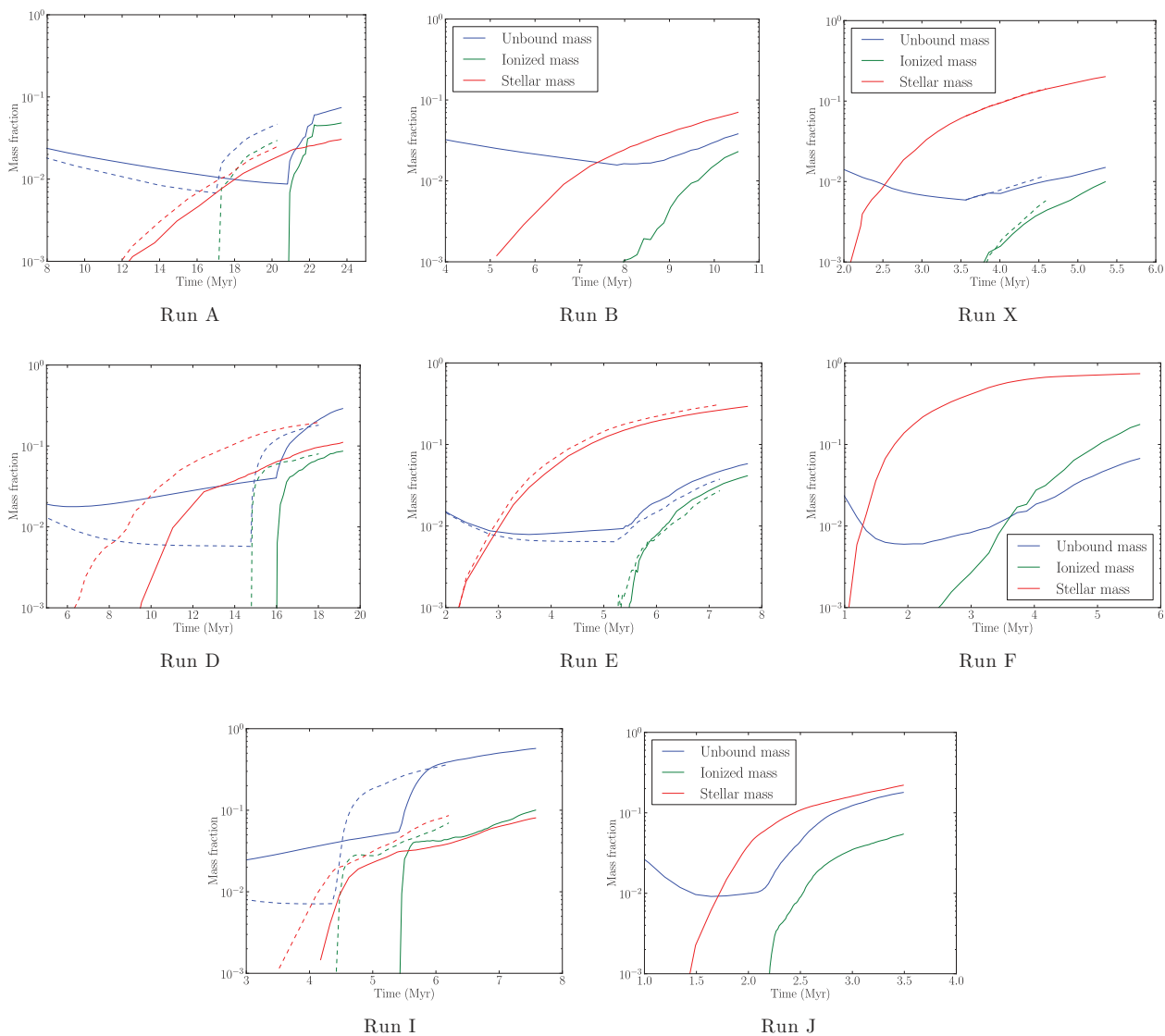


Figure 7. Plots showing the evolution with time of the star formation efficiency (red), ionized gas fraction (green) and unbound mass fraction (blue) in all simulations. Solid lines are for standard runs using the Larson EOS. Dashed lines in Runs A, D, E and I are for runs using an isothermal EOS with a temperature of 10 K. Dashed lines in Run X are from a repeat of part of the simulation from Dale & Bonnell (2011), in which our older, less accurate multiple-source ionization code was used. Note the different horizontal scaling on the plots.

F) than in the systems with lower Mach numbers and densities and warmer temperatures (e.g. Runs D and I). It is also clear that star formation in the low-density, low-Mach number systems is sparse, whereas in the denser and more strongly turbulent clusters such as Runs B, X and F, star formation has been more vigorous and evenly distributed. These are consequences of the higher initial average densities and the higher Mach numbers and stronger shocks in the latter systems.

The subsequent behaviours and morphologies of the clouds are sufficiently diverse that we describe the reaction of each cluster in some detail below. The principal qualitative results may be gleaned from Fig. 7, in which we examine the dynamical reaction of the clouds by plotting their star formation efficiencies, ionization fractions and unbound mass fractions (defined as the fraction of gas with positive total energy, including kinetic, thermal and gravitational components), comparing where appropriate with companion isothermal calculations (shown as dashed lines), and in Fig. 8 where

we show the final states of our calculations, in most cases after ionization has been acting for ~ 3 Myr.

5.1 Run A (mass = $10^6 M_{\odot}$, radius = 180 pc)

This is the largest and most diffuse of our star-forming calculations (since neither Run C nor Run G nor Run H form any stars). The system forms a few tens of widely separated clusters connected by filaments of denser gas from which they continually accrete (Fig. 6). As shown in Fig. 8, photoionization is able to partially disrupt the accretion filaments and creates a network of bubbles, several of which expand outwards from the cloud, becoming champagne flows [an example is visible at about $(-20, -150)$]. The $H II$ regions rapidly join up with one another so that large volumes of ionized gas are being illuminated by several sources. However, much of the volume of the cloud remains untouched by $H II$ gas because the clusters are few and the cloud is very large. Consequently, as we show in Fig. 7,

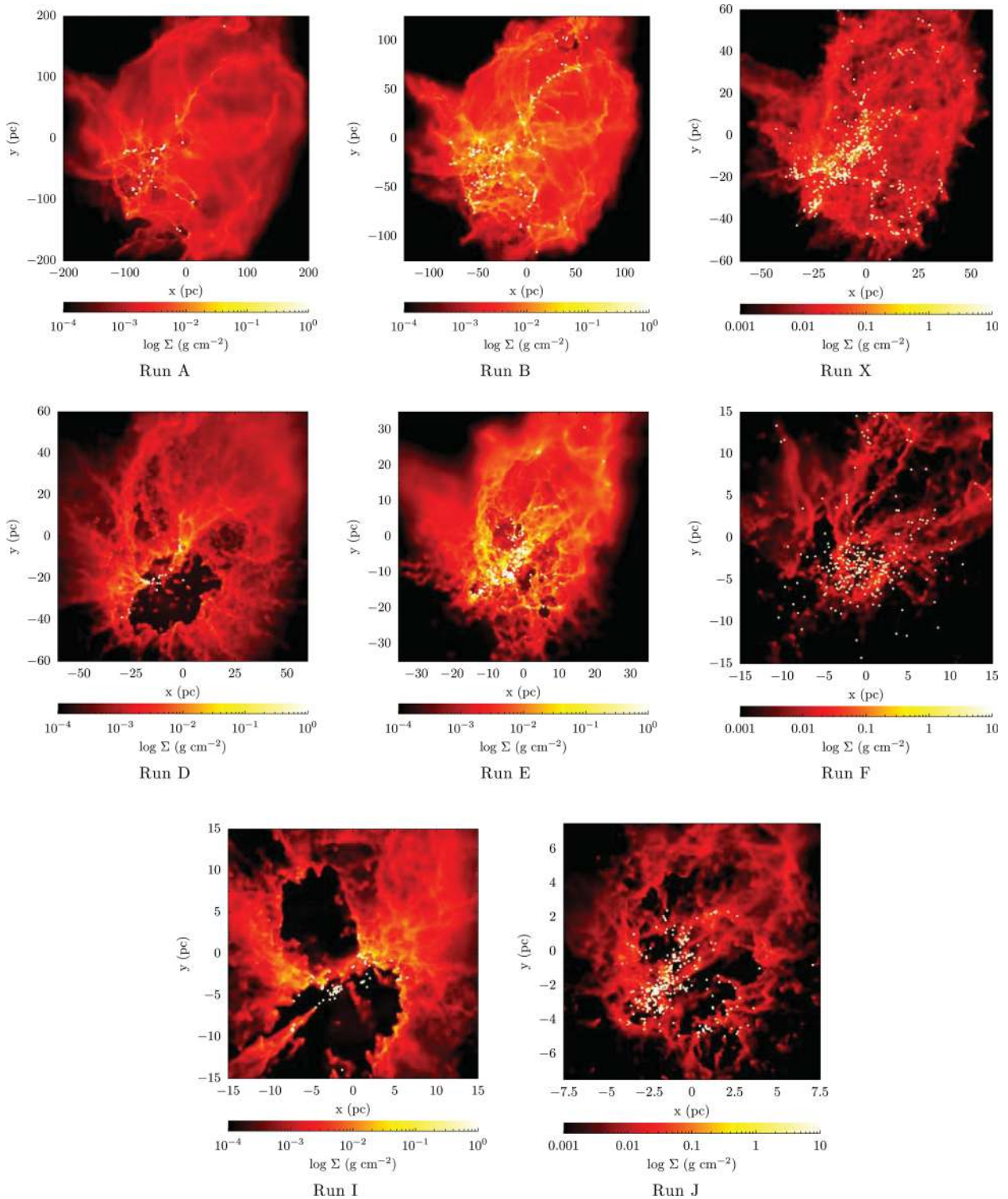


Figure 8. Gallery of final states of clusters, as shown by column density maps observed down the z -axis. White dots represent sink particles (individual stars in Runs I and J, clusters otherwise) and are not to scale. Note the different physical sizes and the different column density scales.

the ionized and unbound gas fractions grow slowly and the effect on star formation, apparent from the flattening of the stellar mass curve, is slight but negative. The evolution of the companion isothermal calculation is very similar. Feedback begins acting earlier owing to the earlier formation of massive clusters in the isothermal calculation, but the quantities of ionized and unbound material extant after 3 Myr of photoionization are very similar, although slightly lower.

5.2 Run B (mass = $10^6 M_{\odot}$, radius = 95 pc)

Star formation in Run B is more vigorous and somewhat less sparse than in Run A, with ~ 100 clusters being formed by the epoch at which ionization was switched on, largely as a consequence of Run B being smaller and denser so that the freefall time is shorter, and the star formation rate per Myr is higher. Owing to the higher

gas densities, most of the ionizing sources are swamped by accretion flows according to the criterion given in equation (5) and the fraction of ionized gas grows more slowly than in Run A. In addition, the escape velocity of Run B is higher than in Run A. The fractions of ionized and unbound gas are able to reach only a few per cent at t_{SN} and the influence on star formation is negligible, as shown in Fig. 7. The morphology of the gas and thus the appearance of the cluster are little affected by feedback, but some disruption of the dense filaments and clearing of material away from some of the clusters has occurred, visible in Fig. 8.

5.3 Run X (mass = $10^6 M_{\odot}$, radius = 45 pc)

This simulation is equivalent to that detailed in Dale & Bonnell (2011), the only difference being that we employ our new more accurate and better physically motivated ionization code. The evolution of the system is very similar to that in the above paper. In Fig. 7 we compare the evolution of the ionized gas fractions, unbound mass fractions and stellar mass using the multiple-source ionization algorithm from Dale & Bonnell (2011) (dashed lines) with Run X (solid lines), in which we use the newer algorithm. The older algorithm produces a very slightly higher ionization fraction, but the difference between the runs is minimal, with the plots of stellar mass fraction being indistinguishable. We confirm that the rate of ionization is very slow due to the strong accretion flows interacting with all the ionizing clusters, with only ~ 1 per cent of the gas being ionized per Myr. The rate at which gas becomes unbound is even lower than in Run B because the escape velocity of the Run X cloud is higher and in fact exceeds the typical sound speed in the ionized gas (this is the only one of our simulations for which this is the case). The effect on the star formation efficiency as a function of time is very small and in Fig. 8, where only neutral gas is shown, there are no discernible morphological signposts of feedback at all.

5.4 Run D (mass = $10^5 M_{\odot}$, radius = 45 pc)

Run D is a diffuse, low- v_{rms} system similar to Run A but considerably smaller. It also forms a few tens of rather sparsely distributed clusters connected by filamentary structures in the gas. Ionization has a much stronger effect on this system, owing to its smaller size and escape velocity, the clusters being distributed over a larger fraction of the system volume, and the weaker accretion flows depositing mass on to them. The bubbles excavated by feedback are of comparable size to those seen in Run A, but, as shown in Fig. 8, occupy a much larger fraction of the volume of the system. The growth of the ionization fraction and influence of feedback on the dynamics are consequently stronger. Fig. 7 shows that ionization is able to unbind more than 25 per cent of the cluster's gas reserves within t_{SN} . However, Fig. 7 also shows that the effect of feedback on the overall star formation rate is minimal. Star formation in the isothermal Run D calculation starts earlier and proceeds to higher efficiencies than in the calculation using the Larson EOS. Feedback therefore also begins acting earlier in the cloud's evolution. However, the fractions of ionized and unbound material resulting from 3 Myr of photoionization in the two calculations are comparable, although somewhat lower in the isothermal case.

5.5 Run E (mass = $10^5 M_{\odot}$, radius = 21 pc)

Run E is similar in structure to Run B at the onset of ionization and, from a dynamical point of view, the evolution of the two systems is similar, although somewhat more material is ionized and

unbound in Run E (Fig. 7). In neither cluster does ionization have any noticeable effect on the star formation rate. However, Fig. 8 shows that photoionization influences the morphology of Run E significantly and is beginning to clear the gas away from the star clusters when the simulation was terminated after 2.3 Myr of feedback – there is a very clearly defined bipolar bubble visible at (7, -20). Run E bridges the gap between the systems towards the high-mass, high-density corner of our parameter space on which feedback has no discernible effect, and the low-mass, low-density corner in which feedback profoundly alters the appearance and dynamics of the clouds. The companion isothermal calculation to Run E is almost identical, with slightly higher star formation efficiency, and slightly lower fractions of ionized and unbound gas.

5.6 Run F (mass = $10^5 M_{\odot}$, radius = 10 pc)

Run F is a small, dense and high- v_{rms} system which, in common with Run J, is unusual in the parameter space in that its freefall time is considerably shorter, at ~ 0.8 Myr, than the critical 3 Myr time window, so that the gravity-driven evolution of Run F proceeds very fast in comparison to this time-scale. The effect of feedback on this cloud is initially very similar to that of Run X in that ionization has minimal impact. The ionized and unbound mass fractions grow very slowly and star formation proceeds largely unrestrained. However, at a system age of ~ 4 Myr ($\sim 5t_{\text{ff}}$), when the star formation efficiency reaches and exceeds 60 per cent, star formation begins to tail off and the ionization fraction begins to grow faster (although the unbound mass fractions evolve largely as before). This change in behaviour is due to the system beginning to run out of gas, clearly illustrated in Fig. 8, but because of star formation and accretion, not because of feedback.

5.7 Run I (mass = $10^4 M_{\odot}$, radius = 10 pc)

Run I has the lowest turbulent Mach number of any of the star-forming systems in this study and its initial filamentary structure is consequently the most poorly defined (Fig. 6) and its density field the smoothest. It also has the lowest escape velocity. As shown in Figs 7 and 8, Run I is the system on which feedback has the most dramatic effect, both dynamically and morphologically. Ionization excavates a vast cavity which appears roughly bipolar in shape when viewed along the z -axis, leaving two separated central clusters entirely devoid of gas, and creating several pillars pointing towards the most massive of the two. After 2.2 Myr, ~ 58 per cent of the gas/stars have been unbound, although the ionization fraction remains modest at ~ 10 per cent. Extrapolating the evolution of the ionization fraction, we conclude that ~ 65 per cent of the system will be unbound by photoionization before the detonation of the first supernova. The effect on the star formation rate is small, although the star formation rate in this system is in any case low. Once again, the isothermal companion run exhibits very similar behaviour. Star formation and feedback both start ~ 1 Myr earlier in the isothermal run, but the evolution of the ionized and unbound gas fractions mirrors that in the standard run, although note that the isothermal calculation was only continued for ≈ 1.9 Myr. As in all the other isothermal simulations, the fractions of ionized and unbound gas are slightly lower than in the standard run.

5.8 Run J (mass = $10^4 M_{\odot}$, radius = 5 pc)

Run J in Fig. 6 appears similar to Run I but with more star formation, owing to its shorter freefall time, and more well-defined filamentary

morphology, due to the higher Mach number of the turbulence. The evolution of Run J is also strongly influenced by feedback. Fig. 8 shows (after only 1.3 Myr) a complex morphology, featuring several poorly defined bubbles and pillar-like structures. Champagne flows were also observed at earlier stages in the evolution. Although we were only able to evolve the system for ~ 1.3 Myr owing to the large number of stars formed (~ 600), Fig. 7 reveals that ionization has already unbound over 18 per cent of the gas by this epoch.

6 DISCUSSION

Our principal goal in this paper was to determine whether photoionization from populations of O-stars or O-star-hosting clusters self-consistently formed within turbulent clouds covering a realistic parameter space could disrupt, or at least strongly dynamically influence the evolution of the clouds before the explosion of the first supernovae. We find that the answer to this question is yes, and our results are summarized in Fig. 9 where we partition our parameter space according to which of our model clouds formed stars and of those which are dynamically influenced by feedback. In the upper region of the plot, populated by Runs C, G and H, our chosen EOS and assumptions about the turbulent velocity dispersion produce clouds whose velocity fields dissipate, and the clouds expand and evaporate, without forming any gravitationally unstable structures. This result is in agreement with the conclusions of Krumholz, Leroy & McKee (2011) who used coupled thermal and chemical models of the ISM to determine the expected correlation between the masses of different ISM phases in a given galaxy, and the total star formation rate. They found that the star formation rate correlates most strongly with the mass of molecular gas, i.e. that most star formation occurs in that phase, and that atomic gas rarely forms stars. This result is also in line with the conclusions of Glover & Clark (2012) who performed detailed thermal and chemical modelling of the ISM to determine whether molecular gas is a prerequisite for star formation to occur. They find that it is not – it is the ability of clouds to self-shield against the external ISM radiation field that determines whether or not they will form stars. Clouds with low surface densities become too warm to form either molecules or stars. This agreement is perhaps not surprising, since Glover & Clark (2012) recovered a temperature–density relation very similar to our assumed EOS.

The lower portion of Fig. 9 containing all our other runs, contains clouds that form stars under the assumptions stated above. If

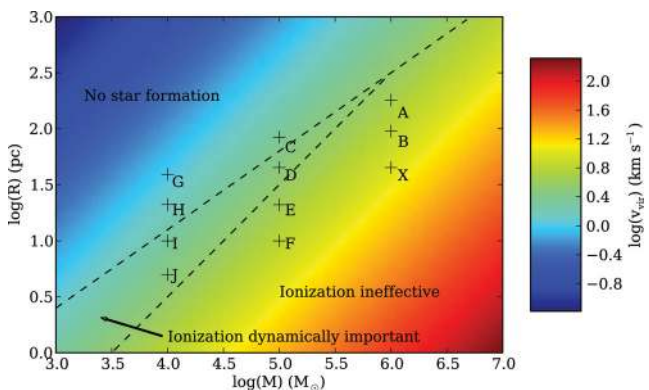


Figure 9. The mass–radius parameter space studied in this work with colours representing cloud turbulent velocities and dashed lines partitioning the mass–radius plane according to whether star formation occurs and whether ionizing feedback is dynamically important.

we define the unbinding of >10 per cent of the system’s mass as constituting a strong dynamical effect, we may divide the lower region in two. The lowest part of the diagram comprising Runs A, B, X, E and F are clusters on which ionizing feedback has little influence within t_{SN} . In the triangular region in between, represented by Runs D, I and J, ionization is able to expel several tens of per cent of the clouds’ gas reserves before any supernovae detonate.

6.1 The dynamical impact of ionization

The different reaction of the clusters to ionization is a consequence of several factors, as detailed in Section 4. In our simulations, the number and luminosity of the ionizing sources plays a minor role inasmuch as it is overwhelmed by other factors. The total ionizing luminosity at the end of Run X is a factor of ≈ 10 times higher than at the corresponding time in Run A but ionization has a much stronger effect on Run A. We also show explicitly in Appendix A that increasing all ionizing luminosities by a factor of 2, or allowing the action of ionization to be earlier when there are fewer sources present have only minor impact on the outcome of a given simulation. The most important factors controlling the evolution of the clouds are their density fields, resulting in turn from their mean densities and turbulent velocity fields, and their escape velocities. The density fields influence photoionization via the accretion rates of the ionizing sources and the recombination rates in the surrounding gas. Using either or of the criteria expressed in equation (3) or (5), the growth of most of the $H II$ regions in Runs X and F, for example, are swamped by accretion – the ionizing fluxes of the sources are unable to keep pace with the inflows of neutral gas delivered by accretion flows – whereas this is not true for any ionizing sources in Runs A, D, I or J. However, Fig. 7 indicates that this is not the most important factor controlling the dynamical influence of ionization. In most of the calculations, the total ionized fraction of the cloud after 3 Myr is in the range 3–10 per cent, yet the unbound mass fractions range from ~ 1 to ~ 60 per cent. Runs E and J, for example, have very similar ionization fractions in their final states of ~ 5 per cent but three times more mass have been unbound in Run J. It is clear that the ability of ionized gas to entrain and expel neutral gas varies greatly across the parameter space, and this is governed by the clouds’ escape velocities. Since the escape velocity depends on the ratio M/R and the clouds in this study and the Heyer et al. (2009) work follow approximately $M \propto R^2$, it follows that larger clouds (in either sense) have higher escape velocities and are thus intrinsically more difficult to unbind with photoionization. It is this factor which is most important in determining how much damage ionization can do to a given cloud.

We note that, in *none* of our model clusters, even those in which large fractions of the neutral gas were swept up and expelled by ionization, is the star formation rate significantly altered in either a positive or negative sense. In the denser higher mass systems such as Runs B, X and F, this is largely due to the fact that ionization has very little effect on the cloud dynamics, so that the star formation process feels no effect. In contrast, in the lower density, lower mass clusters which are strongly influenced by feedback, it appears that the negative impact of losing large fractions of the clouds’ neutral gas is roughly compensated for on the time-scales of these simulations, by positive feedback in the form of triggered star formation. Runs D and I in particular exhibit several features generally associated with triggering such as pillars with stars at their tips and stars embedded in ridges of dense gas around the edges of

feedback-driven bubbles. We defer a detailed study of triggering in these simulations to a later paper.

6.2 Influence of the equation of state

In most of our calculations, we made use of the Larson EOS, as detailed in Section 2. Owing to the large range in densities found in our parameter space, the use of this EOS resulted in some of our clouds being warm enough that they should really be regarded as at least partially atomic, rather than molecular, and we found that these clouds failed to form stars under the influence of our chosen turbulent velocity fields. However, several clouds, e.g. Runs A, D and I were still able to form stars despite their warm average temperatures. To quantify the impact of our assumed EOS, we repeated these simulations (as well as Run E) with an even simpler EOS, namely one with a fixed isothermal temperature of 10 K. In Figs 10 and 11 we show column-density maps of the states of the warm (left-hand panels) and isothermal (right-hand panels) Run I clouds at the time feedback was enabled and after ~ 1.9 Myr of feedback, respectively. The influence of the EOS on the *morphological* evolution of the clouds without feedback is very clear from Fig. 10. There is more fine-scale structure in the isothermal cloud, as would be expected if the average gas temperature is cooler. The morphology of the star formation is rather similar, however, with the main concentration of stars being located at a junction of several filaments of dense gas at approximately $(-3, -4)$ pc in both clouds. This is

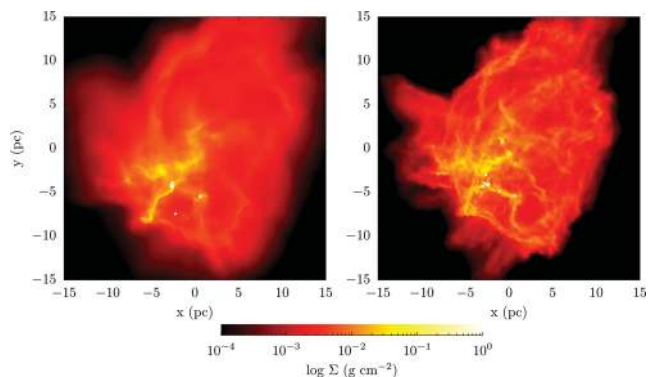


Figure 10. Comparison of the states of the standard (left-hand panel) and isothermal (right-hand panel) Run I calculations at the point where feedback was enabled.

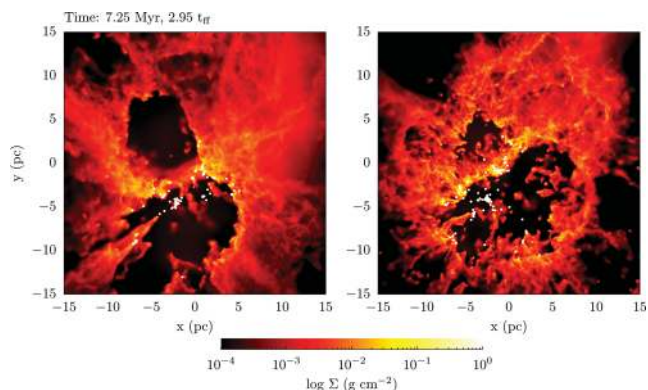


Figure 11. Comparison of the states of the standard (left-hand panel) and isothermal (right-hand panel) Run I calculations after 1.9 Myr of feedback.

largely because the star formation forms in the densest coolest gas, which is treated isothermally in all simulations, and these regions are created by converging turbulent flows, which are also the same in all simulations. Turning to Fig. 11, the effects of feedback on the clouds are also similar. In both cases, the largest stellar concentration located at the filament junction is responsible for most of the ionizing luminosity and generates a roughly bipolar bubble morphology bisected by a ridge of dense material extending roughly diagonally from the lower left to the upper right (at least when viewed in this projection). The bubbles are less symmetrical in the isothermal case, with the upper bubble being much smaller than the lower. In addition, the larger bubble in the isothermal calculation appears to be more spherical in shape and less well cleared out, although this is partly a projection effect. The initially smoother gas in the warm cloud has therefore led to a somewhat simpler bubble morphology. The distribution of stars in the two calculations is also very similar, with both possessing a few well-defined clusters and more distributed star formation in the ridges of dense material.

However, as shown in Section 5, the gross dynamical behaviour of these two simulations is very similar. The temperature of the gas has very little impact on the influence of ionizing feedback. The higher average gas densities in the isothermal calculation result in star formation and feedback beginning earlier but does not much affect the star formation rate or efficiency. This is probably because the isothermal and Larson versions of each simulation have identical turbulent velocity fields and gravitational wells, which between them are what generate the cold gas from which the stars form. The earlier star formation in the isothermal calculations is a result of all the gas being already cool and the shocks being consequently somewhat stronger, but differences in the mean initial gas temperature, unless large enough to make the clouds nearly or actually unbound, do not strongly affect the rate at which cold, dense gas is generated. The mean gas densities in the isothermal calculations are slightly higher than in the standard runs, resulting in a somewhat lower fraction of gas being ionized or unbound at a given time but, as we have seen in all calculations, the depth of the cloud potential well is a much stronger determinant of the impact of feedback.

6.3 Escape of ionizing photons

The source of photons required to maintain the diffuse ionized gas (DIG) layers observed above and below galactic discs is still under discussion. On energetic grounds (e.g. Reynolds 1984), OB stars are strong candidates, but the thickness of such ionized layers is often much greater than that of the thin galactic discs where O-stars are likely to be found. In order for O-stars to accomplish this feat, significant fractions of their photon fluxes must be able to escape their natal molecular clouds, or the O-stars themselves must escape the clouds. Hoopes & Walterbos (2000) attempted to reproduce the DIG characteristics of M33 and concluded that field O-stars could not provide sufficient photons. Both they and Voges & Walterbos (2006) calculated that the DIG in M33 could be explained by a combination of field O-stars and H II regions leaking ~ 30 per cent of their photons into the ISM. There are additional problems with the O-star photoionization model, principally the degree of radiation hardening required to reproduce the observed line ratios (e.g. Wood & Mathis 2004), which are beyond the scope of this paper. However, if OB stars are to be responsible for ionizing the DIG and field O stars cannot do the job alone, GMCs and the H II regions they host must have a high degree of porosity. Fig. 8 suggests that several of our model clouds, particularly those on which feedback has had a

Table 2. Total ionizing photon fluxes, estimated fraction of ionizing photons leaking from clouds and ionizing photon luminosities leaking from each cloud.

Run	Total Q_{H}	f_{phot}	Q_{H}' (10^{49} s^{-1})
A	6.2	0.21	1.3
B	11.2	0.17	1.9
X	38.6	0.07	2.7
D	2.3	0.72	1.7
E	4.1	0.61	2.5
F	18.0	0.88	15.8
I	2.6	0.90	2.3
J	2.2	0.80	1.8

strong influence, may indeed allow large fractions of their ionizing luminosities to escape.

We estimate the escape fractions of ionizing photons at the ends of our simulations as follows: we first allow the multiple-source ionization code to iterate to a solution for the number of ionized particles and the photon fluxes reaching all particles. We then loop through all the ionizing sources, construct a Hammer spherical grid centred on each one, locate the most distant SPH particle in each angular grid cell and compute the flux emerging radially from that particle (if any). We then sum all the emergent fluxes for all sources to compute the total emergent photon flux. In Table 2, we tabulate the total flux of all sources in each simulation, the fraction of these ionizing photons that are escaping f_{phot} and the total flux of photons escaping each cloud, Q_{H}' .

The escape fraction varies widely and broadly in line with how much damage ionization has done to each cloud. With the exception of Run F, all the clouds' apparent ionizing luminosities lie in a very small range, because clouds with the highest actual luminosities have the lowest escape fractions and vice versa. Run F does not follow this trend because alone among the simulated clouds, star formation in Run F has almost gone to completion, so the cloud has both a large number of stars and little remaining gas to absorb their photons. We make no attempt to address the problem of explaining the large observed line ratios in the DIG, but our results do suggest that leakage from H II regions can at least provide sufficient photons.

6.4 Paving the way for supernovae

The simulations presented here have been evolved as close as possible to 3 Myr after the onset of photoionization on the grounds that this is the approximate main-sequence lifetime of the most massive stars, and so that the isolated effect of photoionization may be observed. It is clear from Fig. 8 that the morphology of many of the simulated clouds has been profoundly altered by the action of radiative feedback on this time-scale, so that the environment in which the first supernovae in each cloud detonates has also been affected. A proper understanding of the consequences of this fact requires the simulation of the supernovae themselves, which we defer to later work. The problem in reality is also complicated by the action of winds, which we have neglected here. However, we may gain a crude idea of the impact of subsequent supernovae on our clouds by considering the fate of the momentum (which, unlike energy, cannot leak or be radiated away) injected by each explosion. We take each O-star or O-star-hosting cluster in our simulations to explode spherically symmetrically, ejecting a mass M_{EJECTA} with a total ini-

Table 3. Estimated effects of single supernovae on clouds after the action of photoionization.

Run	f_{esc}	f_{stop}	M_{unbnd} (M_{\odot})
A	<0.01	>0.99	190
B	<0.01	>0.99	180
X	<0.01	>0.99	150
D	0.10	0.90	320
E	0.20	0.80	320
F	0.10	0.90	60
I	0.70	0.30	1990
J	0.65	0.35	1380

tial kinetic energy E_0 , and construct a spherical grid around the explosion site. Each radial bin subtends a solid angle $d\Omega$, contains a mass of cloud material $M(\theta, \phi)$ and absorbs a fraction $d\Omega/4\pi$ of the emitted momentum. We then compute by conserving momentum whether, in each radial bin, the final velocity of the combined ejecta and swept-up mass exceeds the cluster escape velocity. This then gives crude estimates of (i) what fraction f_{esc} of the ejecta escapes the cluster (ii) what fraction f_{stop} of the ejecta is slowed down sufficiently to be involved in further star formation (iii) how much mass M_{unbnd} is likely to be unbound by the explosion (treating each supernova as a separate event and neglecting cumulative effects). If we take $M_{\text{EJECTA}} = 10 M_{\odot}$ and $E_0 = 10^{51}$ erg, we obtain the values given in Table 3.

The interpretation of this crude model should not be taken too far, but Table 3 implies that the porosity of the clouds to supernova ejecta is little affected by ionizing feedback and is instead simply related to the clouds' masses and boundedness. This impression is reinforced by repeating the analysis on the clouds *before* photoionization is switched on, which produces escape fractions only ~ 5 per cent smaller than those given above. The results also suggest that most supernova ejecta in the 10^5 and $10^6 M_{\odot}$ clouds will be retained by the clouds and involved in further star formation, and that the clouds will survive several supernovae. The lower mass clouds, in contrast, will lose most of their supernova ejecta but a small fraction of the original cloud mass ~ 20 per cent is likely to survive both ionization feedback and the first supernova and may host star formation involving chemically enriched material.

6.5 Other forms of feedback

We have considered only the effects of photoionization in this work but in reality, other forms of feedback will act contemporaneously in star-forming regions, even before the detonation of the first supernovae, and these other mechanisms may help or hinder each other in unbinding clouds and expelling material. Winds (spherical outflows) and jets (collimated outflows) also inject energy and momentum into the circumstellar gas. Although jets have lower velocities, they have higher mass-loss rates per star than main-sequence winds and their contribution to clouds' momentum budgets is comparable to or greater than that of winds, but much less than that of H II regions, as shown by Matzner (2002). H II regions are likely to be even more dominant in low-metallicity systems where stellar winds (but not jets) are weak. Numerical simulations by Li & Nakamura (2006) and analytical work by Matzner (2007) found that multiple protostellar jets were able to maintain the supersonic turbulent velocity fields in clouds, although Banerjee, Klessen &

Fendt (2007) arrived at the opposite conclusion from their numerical study. It is not clear, however, whether winds and jets acting together with photoionization will have a greater or lesser effect than any of these mechanisms acting alone. Winds or jets may destroy dense circumstellar material close to ionizing sources, allowing photons to penetrate further into a cloud, but winds may also sweep up low-density material into dense shells which confine H II regions. Conversely, jets are likely to punch holes in any shell-like structures, allowing ionizing photons and hot gas to escape. In their radiation–hydrodynamics simulations of protostellar discs with jets, Cunningham et al. (2011) observed just this phenomenon. Although they themselves make minor contributions to the momentum budget, winds and outflows may potentially alter the effectiveness of the major contributor – the H II regions – but it is not easy to say by how much, or even in which direction.

This question is further complicated by the action of magnetic fields, which we also neglect here. Krumholz, Stone & Gardiner (2007) and Gendelev & Krumholz (2012) simulated the evolution of H II regions in magnetized clouds and found that the energy uptake by the gas was much more efficient than in the unmagnetized case. Wang et al. (2010) found a similar result when comparing simulations including protostellar outflows in the presence and absence of magnetic fields. The magnetic field increases the coherence of outflows and enhances their ability to sweep up material, thereby making them more efficient at expelling circumstellar gas. In the case of H II regions, the efficiency of cloud destruction is still potentially limited by the sound speed in the H II region in the case that the escape velocity of the cloud is comparable or higher. The additional magnetic pressure may lower the effective escape velocity, but the field needs to be rather strong for this to be a large effect.

7 CONCLUSIONS

Ionizing feedback from O-type stars can have a strong dynamical effect on embedded clusters on the 3-Myr time-scale before the first supernovae detonate. The influence of feedback is stifled in clouds with higher densities and more sharply defined structure by the swamping of H II regions by accretion flows. More importantly, clouds with higher escape velocities are more resistant to feedback, since the maximum expansion speed of an H II region is $\sim 10 \text{ km s}^{-1}$. Since observed clouds (and those modelled here) follow approximately the relation $M \propto R^2$, more massive and larger clouds are intrinsically more difficult to unbind. These two factors contribute to making the effects of ionization feedback within the 3-Myr window much stronger on the lower density low-mass ($10^4 M_{\odot}$) clouds than on the densest high-mass $10^6 M_{\odot}$ clouds. That massive clouds with larger escape velocities are difficult or impossible to disrupt by thermal pressure from photoionized gas has been suggested before by Krumholz & Matzner (2009), Murray, Quataert & Thompson (2010) and Fall, Krumholz & Matzner (2010), all of whom posit that in fact radiation pressure is a more important feedback mechanism in high-mass clouds. Our detailed hydrodynamic calculations demonstrate that this is indeed the case.

The influence of ionizing feedback on the rate and efficiency of star formation was small in all our model clusters, either through the general inability of feedback to perturb the more massive and denser clouds, or through an approximate cancelling of disruption and triggering in the low-mass more diffuse systems, which we will explore in detail in a subsequent paper. Overall, the fact that stars form in the densest gas, often pre-existing thanks to the turbulence with which the clouds were seeded, limits the effect.

The lower mass and lower density clouds become highly porous to ionizing photons due to the influence of feedback, but overall (with the exception of the gas-deprived Run F), the effective ionizing luminosities of all the clouds are the same to within a factor of ~ 2 because the more porous clouds are also those with the smaller numbers of O-stars. Given that low-mass clouds are more common than high-mass ones, this results implies that most photons in the ISM which were produced by O-stars come from low-mass clouds.

The low-mass clouds are also porous to supernova ejecta, but this is not much aided by the action of photoionization. 60–70 per cent of the ejecta from the $10^4 M_{\odot}$ clouds should be returned directly to the ISM, while the rest is likely to become involved in a second round of star formation in the remains of the clouds. In the higher mass clouds, most of the supernova ejecta should become involved in further star formation.

Morphologically, our simulations exhibit virtually every feature commonly associated with feedback. We see evacuated cavities with pillars containing young stellar objects pointing towards massive stars similar to those seen in the Eagle Nebula (e.g. Sugitani et al. 2002), bubbles reminiscent of those observed by Churchwell et al. (2006) and champagne flows like that detailed by Maheswar et al. (2007). However, we note that these are qualitative comparisons based on our simplistic column-density plots. In a later work, we will perform artificial observations of our results in commonly used emission lines such as O[III] and N[II] that may be more quantitatively compared with observations.

The next steps in this work are to examine in detail the triggering of star formation within the clouds, to extend the parameter space to initially unbound clouds, to include the effects of stellar winds and to simulate the effects of supernovae.

ACKNOWLEDGMENT

The authors thank the anonymous referee for careful and constructive criticism which has significantly improved the paper.

REFERENCES

- Allison R. J., Goodwin S. P., Parker R. J., de Grijs R., Portegies Zwart S. F., Kouwenhoven M. B. N., 2009, *ApJ*, 700, L99
 André P. et al., 2010, *A&A*, 518, L102
 Banerjee R., Klessen R. S., Fendt C., 2007, *ApJ*, 668, 1028
 Bate M. R., Bonnell I. A., Price N. M., 1995, *MNRAS*, 277, 362
 Benz W., 1990, in Buchler J. R., ed., *Numerical Modelling of Nonlinear Stellar Pulsations: Problems and Prospects*. Kluwer, Dordrecht, p. 269
 Bodenheimer P., Tenorio-Tagle G., Yorke H. W., 1979, *ApJ*, 233, 85
 Boily C. M., Kroupa P., 2003a, *MNRAS*, 338, 665
 Boily C. M., Kroupa P., 2003b, *MNRAS*, 338, 673
 Bonnell I. A., Vine S. G., Bate M. R., 2004, *MNRAS*, 349, 735
 Churchwell E. et al., 2006, *ApJ*, 649, 759
 Cunningham A. J., Klein R. I., Krumholz M. R., McKee C. F., 2011, *ApJ*, 740, 107
 Dale J. E., Bonnell I., 2011, *MNRAS*, 414, 321
 Dale J. E., Bonnell I. A., Clarke C. J., Bate M. R., 2005, *MNRAS*, 358, 291
 Dale J. E., Ercolano B., Clarke C. J., 2007, *MNRAS*, 382, 1759
 Diaz-Miller R. I., Franco J., Shore S. N., 1998, *ApJ*, 501, 192
 Dobbs C. L., Burkert A., Pringle J. E., 2011, *MNRAS*, 413, 2935
 Ercolano B., Barlow M. J., Storey P. J., Liu X.-W., 2003, *MNRAS*, 340, 1136
 Ercolano B., Barlow M. J., Storey P. J., 2005, *MNRAS*, 362, 1038
 Ercolano B., Young P. R., Drake J. J., Raymond J. C., 2008, *ApJS*, 175, 534
 Fall S. M., Krumholz M. R., Matzner C. D., 2010, *ApJ*, 710, L142
 Gendelev L., Krumholz M. R., 2012, *ApJ*, 745, 158

- Glover S. C. O., Clark P. C., 2012, MNRAS, 421, 9
 Glover S. C. O., Mac Low M.-M., 2007, ApJ, 659, 1317
 Glover S. C. O., Federrath C., Mac Low M.-M., Klessen R. S., 2010, MNRAS, 404, 2
 Goldbaum N. J., Krumholz M. R., Matzner C. D., McKee C. F., 2011, ApJ, 738, 101
 Goodwin S. P., 1997, MNRAS, 284, 785
 Goodwin S. P., Bastian N., 2006, MNRAS, 373, 752
 Heyer M., Krawczyk C., Duval J., Jackson J. M., 2009, ApJ, 699, 1092
 Hill T. et al., 2011, A&A, 533, A94
 Hills J. G., 1980, ApJ, 235, 986
 Hoopes C. G., Walterbos R. A. M., 2000, ApJ, 541, 597
 Koyama H., Inutsuka S. I., 2000, ApJ, 532, 980
 Krumholz M. R., Matzner C. D., 2009, ApJ, 703, 1352
 Krumholz M. R., Matzner C. D., McKee C. F., 2006, ApJ, 653, 361
 Krumholz M. R., Stone J. M., Gardiner T. A., 2007, ApJ, 671, 518
 Krumholz M. R., Leroy A. K., McKee C. F., 2011, ApJ, 731, 25
 Lada C. J., Lada E. A., 2003, ARA&A, 41, 57
 Larson R. B., 1985, MNRAS, 214, 379
 Larson R. B., 2005, MNRAS, 359, 211
 Li Z.-Y., Nakamura F., 2006, ApJ, 640, L187
 McMillan S. L. W., Vesperini E., Portegies Zwart S. F., 2007, ApJ, 655, L45
 Maheswar G., Sharma S., Biman J. M., Pandey A. K., Bhatt H. C., 2007, MNRAS, 379, 1237
 Matzner C. D., 2002, ApJ, 566, 302
 Matzner C. D., 2007, ApJ, 659, 1394
 Mazurek T. J., 1980, A&A, 90, 65
 Men'shchikov A., André P., Didelon P., Könyves V., Schneider N., Motte F., Bontemps S., Arzoumanian D., 2010, A&A, 518, L103
 Moeckel N., Bonnell I. A., 2009, MNRAS, 396, 1864
 Monaghan J. J., 1992, ARA&A, 30, 543
 Murray N., Quataert E., Thompson T. A., 2010, ApJ, 709, 191
 Myers P. C., 1978, ApJ, 225, 380
 Peters T., Mac Low M., Banerjee R., Klessen R. S., Dullemond C. P., 2010, ApJ, 719, 831
 Reynolds R. J., 1984, ApJ, 282, 191
 Schmutzler T., Tscharnuter W. M., 1993, A&A, 273, 318
 Solomon P. M., Sanders D. B., Scoville N. Z., 1979, in Burton W. B., ed., Proc. IAU Symp. 84, The Large-Scale Characteristics of the Galaxy. Reidel, Dordrecht, p. 35
 Solomon P. M., Rivolo A. R., Barrett J., Yahil A., 1987, ApJ, 319, 730
 Sugitani K. et al., 2002, ApJ, 565, L25
 Tenorio-Tagle G., 1979, A&A, 71, 59
 Vázquez-Semadeni E., Colín P., Gómez G. C., Ballesteros-Paredes J., Watson A. W., 2010, ApJ, 715, 1302
 Voges E. S., Walterbos R. A. M., 2006, ApJ, 644, L29
 Walch S., Whitworth A., Bisbas T., Hubber D. A., Wuensch R., 2011, arXiv e-prints
 Walmsley M., 1995, Rev. Mex. Astron. Astrofis. Conf. Ser., 1, 137
 Wang P., Li Z.-Y., Abel T., Nakamura F., 2010, ApJ, 709, 27
 Whitworth A., 1979, MNRAS, 186, 59
 Williams J. P., McKee C. F., 1997, ApJ, 476, 166
 Wolfire M. G., Hollenbach D., McKee C. F., Tielens A. G. G. M., Bakes E. L. O., 1995, ApJ, 443, 152
 Wood K., Mathis J. S., 2004, MNRAS, 353, 1126
 Yorke H. W., Tenorio-Tagle G., Bodenheimer P., Rozyczka M., 1989, A&A, 216, 207

APPENDIX A:

In this section, we detail some additional simulations performed to test the influence of some of the assumptions made in our models. Most of these tests were conducted on Run E, since it lies in the middle of the parameter space, near the approximate demarcation line between systems that are and are not strongly affected by photoionization.

A1 Effect of increasing the ionizing luminosity

In most of our simulations, the sink particles represent small clusters rather than individual stars and the ionizing luminosity must therefore be estimated from each cluster's mass using an initial mass function (IMF). This involves making assumptions about the IMF slope and lower mass cut-off, which determines how much mass in a given cluster is locked up in OB-type stars, and computing from this mass an ionizing luminosity. Given that the most massive sink particles representing clusters, even in our $10^6 M_{\odot}$ clouds, have masses of typically only a few thousand M_{\odot} , the upper ends of their IMFs will be poorly sampled and only a simple estimate of their ionizing luminosities is appropriate. However, in Runs I and J, we resolve individual stars and Run J has a reasonably well-sampled IMF containing ~ 700 objects by the end of that simulation. The total stellar mass at the end of Run J is $\sim 2400 M_{\odot}$ and the total ionizing photon flux is $2.2 \times 10^{49} \text{ s}^{-1}$. If the formula detailed in Section 2 is used to compute the photon flux of a $2400 M_{\odot}$ cluster, the result obtained is $0.9 \times 10^{49} \text{ s}^{-1}$, or about half as luminous. To compute the luminosity of our unresolved clusters, we integrate over an assumed Salpeter IMF between mass limits of 0.1 and $100 M_{\odot}$ to compute the total mass in stars whose mass exceeds $30 M_{\odot}$, whereas the mass resolution in Run J is $\sim 0.5\text{--}1 M_{\odot}$. In Fig. A1 we confirm that the mass functions in Runs I (blue) and J (green) are well fit by the Salpeter power law, depicted by the red line. If we were instead to use 0.5 or $1.0 M_{\odot}$ as the lower IMF mass limits, our unresolved clusters would be, respectively, 1.9–2.6 times more luminous. Taking a factor of 2 to be a reasonable uncertainty in our cluster photon fluxes, we therefore repeated Run E with the luminosities of all clusters increased by a factor of 2. The result of the simulation is shown in Fig. A2, compared to the standard computation with the original luminosities. We see that, initially, the quantity of ionized material in the calculation with enhanced luminosities is approximately a factor of 2 larger than in the standard run. This is to be expected, since the Strömgren radius is proportional to $Q_{\text{H}}^{1/3}$ and the volume of initially ionized material is therefore proportional to Q_{H} . However, the differences in both ionized and unbound mass between the two simulations do not grow but instead shrink with time and the overall evolution of the runs is very similar. Uncertainties of a factor of a few in the ionizing fluxes of sources are less important

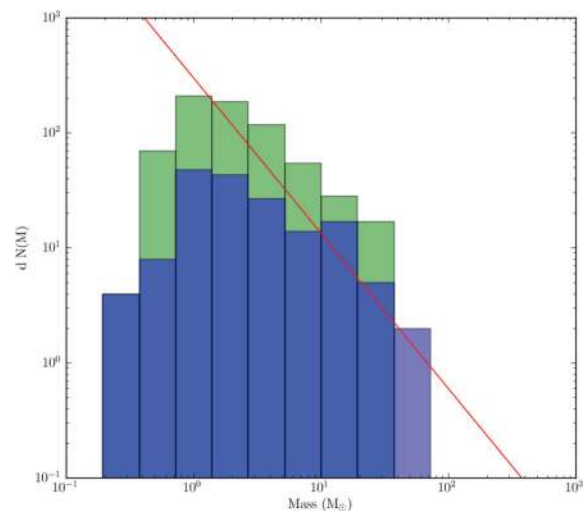


Figure A1. Comparison of the stellar mass functions in Run I (blue) and Run J (green), with the Salpeter mass function (red line).

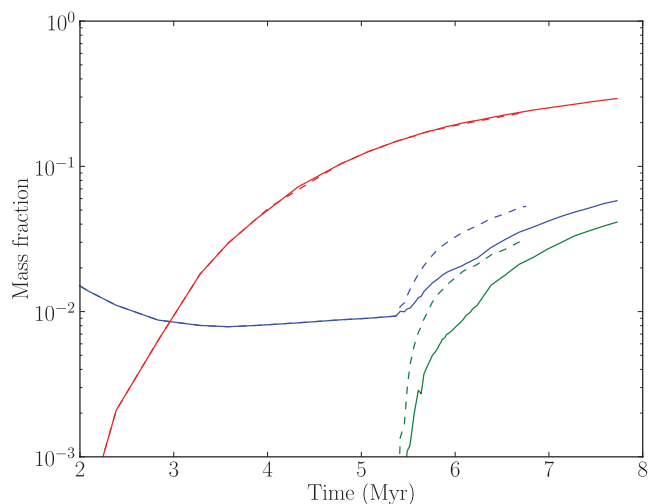


Figure A2. Comparison of the evolution of the standard (solid lines) Run E with a duplicate run in which all ionizing photon fluxes are twice as big (dashed lines).

to the evolution of the clouds than the potential well in which the H II regions are trying to expand.

A2 Effect of switching ionization on earlier

This study aims at a better understanding of the large-scale impact of multiple ionizing sources on star-forming regions. The ionizing photon flux is dominated by the few most massive sources, and is therefore potentially subject to stochastic effects. To lessen these effects, we allowed our model clouds to develop a small number of sources massive enough to possess ionizing fluxes before enabling feedback. To quantify such effects, we repeated Runs D and E, enabling feedback as soon as the first object became sufficiently massive. The results are shown in Figs A3 and A4 compared with the standard runs in both cases. In the case of Run D, this results in feedback beginning ~ 3 Myr earlier in the system's evolution (equivalent to ~ 0.45 freefall times). The result is a considerably smaller mass of material being ionized, reducing the global ionization fraction after 3 Myr of feedback from ~ 9 to ~ 2 per cent.

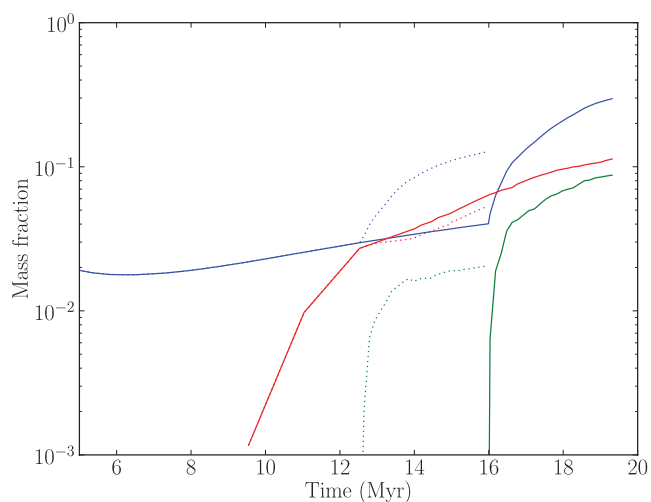


Figure A3. Comparison of the evolution of the standard (solid lines) Run D with a duplicate in which ionization is enabled as soon as is possible (dashed lines).

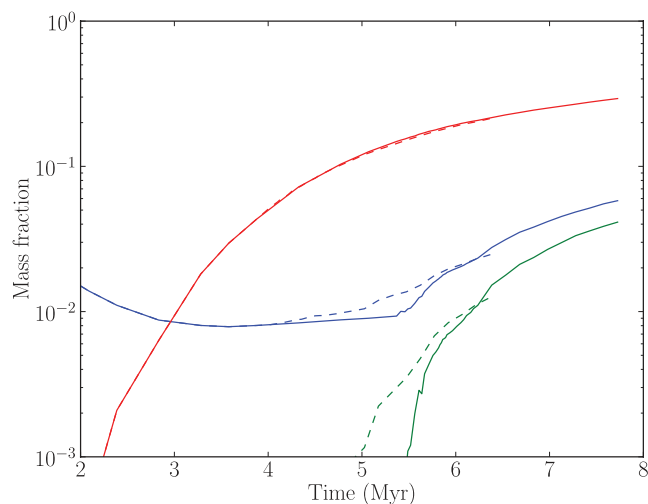


Figure A4. Comparison of the evolution of the standard (solid lines) Run E with a duplicate in which ionization is enabled as soon as is possible (dashed lines).

However, the difference in the amount of material unbound on the same time-scale is only a factor of 2 – ~ 15 per cent as opposed to ~ 30 per cent. The impact on Run E is rather similar. Feedback is enabled ~ 1.5 Myr earlier (~ 0.60 freefall times), resulting in the ionization fraction after 2.3 Myr of feedback being reduced by a factor of ~ 4 and the unbound gas fraction being reduced by a factor of ~ 2 . Exactly when feedback begins acting on a cloud clearly has some influence on the evolution but varying this time by substantial fractions of the system freefall time produces only modest differences in the quantities of material unbound.

A3 Effect of numerical resolution

To evaluate the influence of numerical resolution, we simply randomly dispensed with half the SPH particles in the initial conditions (reducing the particle number to 5×10^5) for Run E and repeated the simulation. We show the results in Fig. A5 as dashed lines

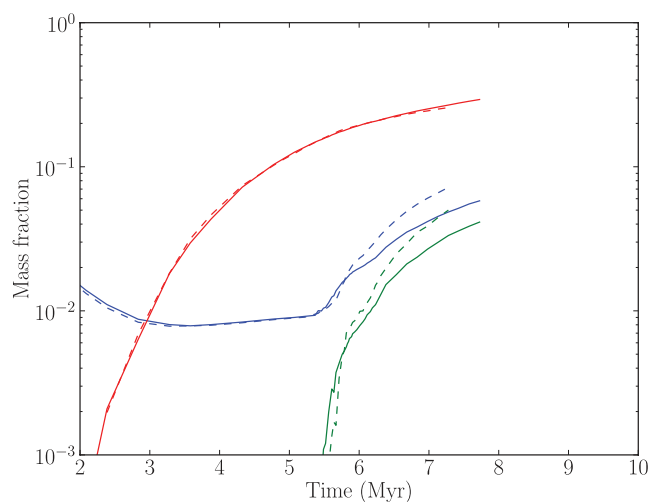


Figure A5. Comparison of the evolution of the standard (solid lines) 10^6 -particle Run E with a duplicate low-resolution 5×10^5 -particle run (dashed lines).

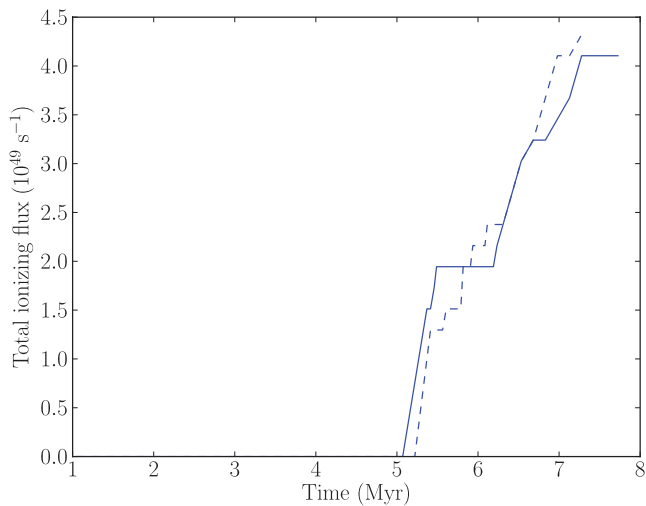


Figure A6. Comparison of the total ionizing fluxes as functions of time in the standard (solid lines) and low-resolution (dashed lines) Run E.

compared with the original 10^6 particle calculation shown as solid lines. The lower resolution simulation has slightly lower fractions of ionized and unbound gas in the earlier stages of the simulation and slightly higher fractions in the later stages, although the stellar mass fractions are virtually identical. The reason for the differences is largely due to differences in the total ionizing luminosities in the two calculations, shown in Fig. A6 – the total luminosity in the low-resolution simulation is somewhat lower in the early phases of the calculation, but transitions to being the same as, or higher than, the luminosity in the standard run at later times. This is due simply to the slightly different history of cluster formation and mergers in the two simulations and illustrates how small-number statistics of the few ionizing sources can have some influence on the outcome of simulations, but the difference in the results is not large enough to be significant.

This paper has been typeset from a $\text{\TeX}/\text{\LaTeX}$ file prepared by the author.